Investigation of Rayleigh-Taylor Instabilities using High-Order FEM

Qasim Ebsim

Dr. Pierre F. J. Lermusiaux
Professor of Mechanical Engineering and Ocean Science and Engineering
Massachusetts Institute of Technology

Aditya K. Saravanakumar
Corbin Foucart
Graduate Students
Massachusetts Institute of Technology

Abstract

Accurate and computationally tractable ocean solvers have diverse applications. One phenomenon these solvers are used to simulate is Rayleigh-Taylor instabilities (RTIs) which can occur in oceans when colder water is dragged on top of warmer water and then pulled down due to gravity. The same phenomenon can similarly be observed at a smaller lab scale in which a heavier fluid sits on a less dense fluid. In this work, we demonstrate the capability of our in-house C++ ocean solver to capture lab-scale RTI flows. We observe significant changes to the domain size of the simulation result in the Courant–Friedrichs–Lewy (CFL) condition being violated. We also note that the momentum diffusion plays a significant role in counteracting these violations. We also examine the significance of the tracer diffusivity and how large diffusivity values can oppose the progression of RTIs. Finally, this paper demonstrates how the vertical forcing term due to density difference plays a dynamically significant role in the lab scale domain when compared to the ocean scale domain. We also identify a non-dimensional number to characterize the importance of this vertical forcing term.

Summary

In this paper, we simulate Rayleigh-Taylor instabilities, a phenomenon that occurs when a dense fluid pushes down on a lighter fluid, using an ocean solver in a lab-scale setup. We examine the required condition such that the solver produces a viable solution as well as examining when the vertical buoyancy force is significant.

1 Introduction

Computationally tractable fluid simulators which predict the movement of ocean currents hours in advance have uses from autonomous vehicles [1] to environmental studies [2]. This paper aims to use one such computational fluid dynamics numerical solver to simulate and investigate nonhydrostatic, density-driven Rayleigh-Taylor instabilities (RTIs).

RTIs are a phenomenon that occurs when a denser fluid pushes into a less dense fluid [3]. These instabilities are observed in processes that span a wide range of length scales ranging from supernova explosions [4] to turbulence mixing.[5, 6]. As can be seen in Figure 1, these instabilities are often characterized by steep gradients in the density field, and as such, can be accurately captured by a discontinuous representation of the numerical solution to the Navier-Stokes equations, see Figure 1, (Right). The numerical methods considered in this work are discontinuous Galerkin finite element methods with a free surface, which will be introduced in §2.3.
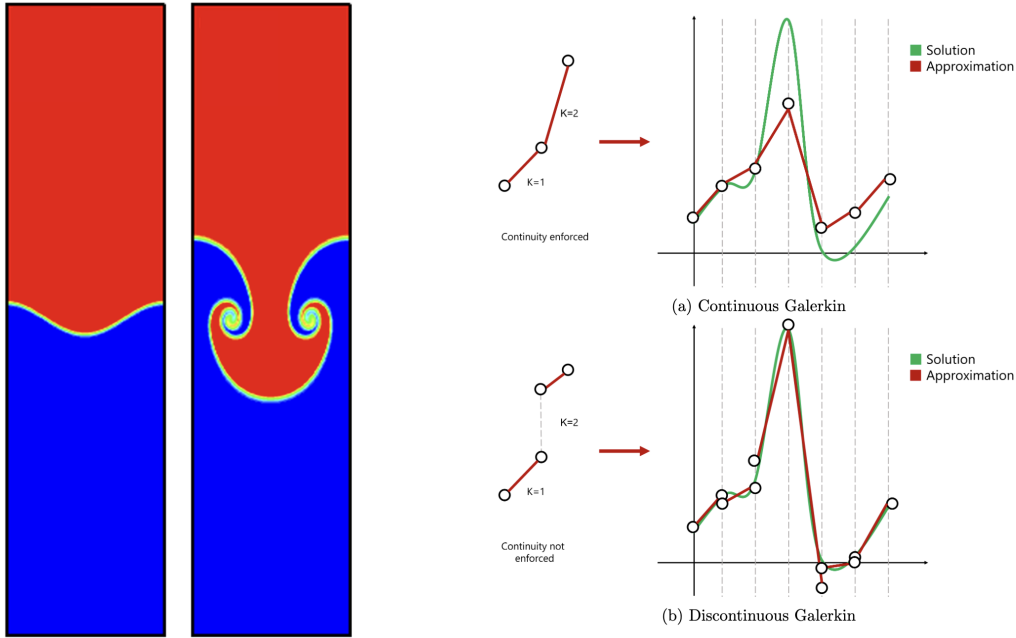

Figure 1: (Left) Rayleigh-Taylor Instability [3] driven by the presence of denser fluid over lighter fluid. (Right) Continuous and discontinuous numerical representations of a continuous solution[7].

While it has been demonstrated that an HDG-based solver is capable of capturing large-scale ocean dynamics [8], the use of these state-of-the-art solvers to investigate fluid motions that occur at

smaller, laboratory scales is as of yet uninvestigated. Ocean-scale processes occur at scales where horizontal motions are much larger than those in the vertical due to the aspect ratio of ocean domains (typically thousands of kilometers in the horizontal but only a few hundred meters in the vertical). Laboratory-scale fluid physics, on the other hand, has horizontal and vertical length scales on the same order of magnitude. Assumptions of vertical rigidity imparted by the aspect ratios encountered on ocean scales are no longer valid, and at these smaller scales, the physical processes driving the dynamics in the fluid are different.

2 Background

2.1 Mathematical Model

In this paper, we consider the non-hydrostatic ocean equations with a free surface on a two dimensional domain $\Omega \subset \mathbb{R}^d$, derived from the incompressible Navier–Stokes equations with the Boussinesq approximation in a rotating reference frame[8]:

$$\frac{\partial \boldsymbol{u}}{\partial t} - \nabla \cdot (\nu \nabla \boldsymbol{u}) + \nabla \cdot (\boldsymbol{u} \otimes \boldsymbol{u}) + \nabla p' + g \nabla_{xy} \eta + \frac{1}{\rho_0} \int_z^\eta g \nabla_{xy} \rho' \, dz' = -\boldsymbol{f}_{\text{cor}} + \frac{\alpha}{\rho_0} \boldsymbol{f}_\rho \qquad (1)$$

$$\nabla \cdot \boldsymbol{u} = 0 \qquad (2)$$

$$\frac{\partial \eta}{\partial t} + \nabla \cdot \left(\int_{-H}^\eta \boldsymbol{u} \, dz \right) = 0 \qquad (3)$$

$$\frac{\partial \rho'}{\partial t} - \nabla \cdot \left(\kappa \nabla \rho' \right) - \nabla \cdot \left(\boldsymbol{u} \rho' \right) = f_{\rho'} \qquad (4)$$

where the unknowns are the velocity $\boldsymbol{u} = (u_1, \ldots, u_d)^T$, the nonhydrostatic pressure p', the density perturbation ρ', and the free-surface elevation η defined over the top surface of the domain boundary $\partial \Omega_\eta \subset \mathbb{R}^{d-1}$, which coincides with the surface $z = 0$ in this work. The domain configuration is illustrated schematically in Figure 2. The quantity $\nu \in \mathbb{R}^{d \times d}$ is a diagonal second-order tensor describing the direction-dependent kinematic viscosity. Similarly, $\kappa \in \mathbb{R}^{d \times d}$ describes the direction-dependent tracer (density) diffusivity. We denote the depth of the bathymetry, the depth of water, as the positive quantity $H(x)$. However, as this paper considers a lab set-up, we assume for the depth to be constant as would be absorbed rectangular tank. The density perturbation is defined
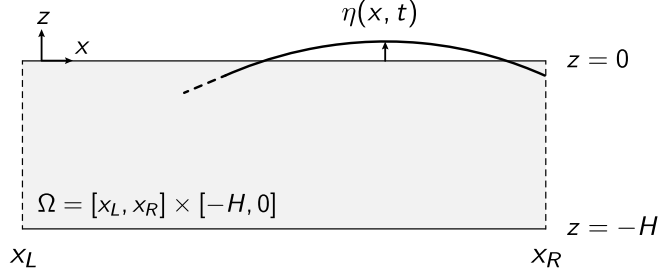
Figure 2: Schematic of the 2-dimensional computational domain Ω. We consider Ω to exist for $\{x_L \leq x \leq x_R\}$ and $\{0 \leq z \leq -H\}$

in relation to the background density such that the total density $\rho = \rho_0 + \rho'$. The nonhydrostatic pressure is defined in relation to the total pressure and density

$$p = p_{\text{hyd}} + \rho_0 p', \qquad p_{\text{hyd}} = \int_z^\eta \rho_0 g \, dz'. \tag{5}$$

Although the governing equations are written for arbitrary spatial dimensions, in this report, we will specifically consider two-dimensional problems with $d = 2$. We will refer to the velocity in the $\hat{z}$ as w, and the velocity field as $\boldsymbol{u} = (u, w)$. Similarly, we define the horizontal velocity $\mathbf{u} = u$. The scalar $\alpha \in \{0, 1\}$ can be thought of as an indicator variable for whether the model should include explicit forcing in the vertical due to buoyancy; this is discussed in §2.2.

2.2 The Boussinesq approximation and vertical density forcing

The dynamics captured in the simulation are a direct consequence of the underlying mathematical model. The ocean equations above are formulated in terms of the nonhydrostatic perturbation quantities p' and ρ', the nonhydrostatic pressure and density perturbations, respectively. That is to say, the equations have been formulated to solve for perturbations away from a hydrostatic equilibrium. However, there is a question as to how to define the hydrostatic pressure; an alternate definition to that of (5) is to consider a hydrostatic pressure which contains the full density: $p_{\text{hyd}} = \int_z^\eta \rho_0 + \rho'(\boldsymbol{x}) \, dz'$. In that case, the gradient of the hydrostatic pressure will cancel the vertical density forcing term due to the hydrostatic approximation which assumes the vertical forcing term to be negligible, resulting in $\alpha = 0$ in (6) and the disappearance of that term in the momentum

3

equation. We will refer to the model in which the hydrostatic approximation is made as the "non-explicitly forced" model, and the formulation following from the definition in (5) as the "explicitly-forced" model. The vertical momentum equation is affected by the addition of this "forcing term", and enters the numerical scheme through the predictor velocity. The velocity predictor calculates the new velocity field but does not take the incomprehensibility of the liquid into account and needs to go through a Helmholtz decomposition to return it back into the space of valid values. We provide the complete temporal discretization of the projection method in §A, but show the predictor velocity in (6). The predictor velocity $\bar{\boldsymbol{u}}^{k+1} = [\bar{u}, \bar{w}]$ equations follow directly from the momentum equations, with the viscous diffusion terms treated implicitly; the nonlinear advective terms and forcing terms are treated explicitly.

$$
\frac{\partial \bar{u}^{k+1}}{\partial t} - \frac{\partial}{\partial x}\left(\nu_x \frac{\partial \bar{u}^{k+1}}{\partial x}\right) - \frac{\partial}{\partial z}\left(\nu_z \frac{\partial \bar{u}^{k+1}}{\partial z}\right)
$$
$$
= -\frac{\partial p'^{,k}}{\partial x} - g\frac{\partial \eta^k}{\partial x} - \frac{g}{\rho_0}\int_z^{\eta^k} \frac{\partial \rho'^{,k}}{\partial x}\,dz' - \nabla\cdot\left(u^k \otimes \boldsymbol{u}^k\right) - \frac{1}{\rho_0}f_x
$$
$$
\frac{\partial \bar{w}^{k+1}}{\partial t} - \frac{\partial}{\partial x}\left(\nu_x \frac{\partial \bar{w}^{k+1}}{\partial x}\right) - \frac{\partial}{\partial z}\left(\nu_z \frac{\partial \bar{w}^{k+1}}{\partial z}\right) = -\frac{\partial p'^{,k}}{\partial z} - \nabla\cdot\left(v^k \otimes \boldsymbol{u}^k\right) - \underbrace{\alpha\frac{\rho'^{,k}}{\rho_0}g}_{\text{vertical forcing}} - \frac{1}{\rho_0}f_z
$$

(6)

The additional vertical forcing term $\rho'^{,k}g/\rho_0$ has been retained in the vertical momentum equation by removing the contribution due to the density perturbation in (5). We remark that the choice to include or exclude the density perturbation in the definition of the hydrostatic pressure is both valid and depends on the modeling goals at hand. As we will see in this report, while unimportant at oceanic scales, the inclusion of the vertical forcing term in the momentum equation is crucial for capturing laboratory-scale RTI phenomena.

2.3 Finite Element Method

2.3.1 Introduction to FEMs

As discussed in §2 the Navier-Stokes equations are a set of partial differential equations (PDEs) that describe the motion of Newtonian fluids such as water. Accurate approximate solutions can be obtained through the use of numerical solvers to predict the motion of afluid given its initial conditions (ICs) and boundary conditions (BCs).

Finite element methods (FEMs) are a class of methods that discretize the underlying PDE and

search for the solution in a known functional space. FEMs discretize the continuous problem into a set of unknown nodal degrees of freedom, the number of which affects the resolution and accuracy of the simulation.

2.3.2 Introduction to HDG

The simulation used in this paper uses the hybridizable discontinuous Galerkin finite element Method (HDG-FEM). Compared to the more commonly used Continuous Galerkin (CG) FEM, HDG is based on the Discontinuous Galerkin (DG) method as it provides greater flexibility and accuracy.
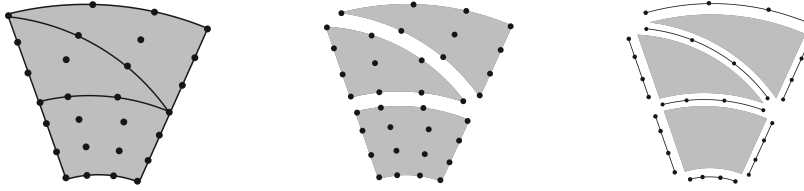
Figure 3: Representation of the discretization of a 2-dimensional domain. CG- (left), DG- (middle), and HDG-FEM (right).

The advantages of DG-FEM are tempered by the duplicated degrees of freedom at the element edges, resulting in a larger number of problem degrees of freedom; this results in a more computationally expensive method. HDG finite element methods, in contrast, parameterize the entire problem onto a mesh "skeleton" space, substantially reducing the number of globally-coupled degrees of freedom, while retaining a full DG-FEM solution representation. The differences between the finite element spaces considered in classical CG-FEM, DG-FEM, and HDG-FEM are depicted in Figure 3.

3   Numerical Experiments and Results

3.1   Initial Attempts

The initial attempts devolved into instability quickly, these resulted from growing oscillation forming in the floating point values as their magnitude grow. These tests featured an ocean level scale,

3 km along the x-axis and 5 km along the z-axis. The initial density perturbation, ρ' was calculated by determining whether points lay above or below the critical height, $H_{\text{critical}}(x)$.

$$\rho'(x,y) = \begin{cases} 2 & \text{if } y < H_{\text{critical}}(x) \\ 0 & \text{if } y \geq \rho'(x) \end{cases} \tag{7}$$

where,

$$H_{\text{critical}}(x) = -\tanh\left[\frac{(x - \frac{L}{2})^2}{N}\right] \cdot M - \frac{H}{2} \tag{8}$$

The critical height's, $H_{\text{critical}}(x)$, shape is controlled through N and M. M is directly related to the depth of the perturbation while N controls the perturbation's width. However, due to a lack of resolution as shown in 4a, the perturbation had irregularities.

Due to a lack of many other refinements, the initial runs all developed major errors before 10 timesteps. The lack of stability could be clearly seen after a few time steps, as is seen in 4b. While the general behavior of RTIs can be seen, this trial showed that going forward, it would be better to reduce domain size to better focus on the key issues.
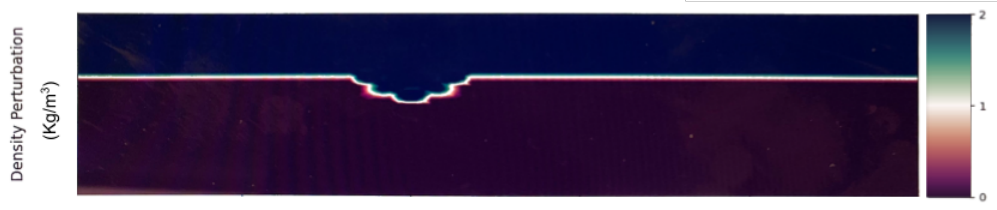
(a) Initial condition at t=0.0s, the initial perturbation function can be seen along with the resolution errors
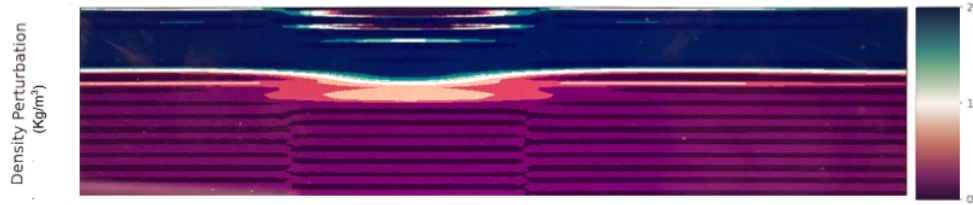
(b) Numerical errors are clearly visible at t=0.9s

Figure 4: Contour plots of the density perturbation for initial trials with domain of 3000 m by 5000m. $\rho' = 2$ and $\Delta t = 0.1s$

3.2 Boundaries

RTIs can easily be viewed in a lab environment by placing a denser liquid on top of a lighter liquid in a closed container. By setting the simulation up such that it resembles a closed container, the only factors that affect the flow of the simulations are those we are trying to observe. In a closed container, the velocity across the boundary should be 0. This type of boundary condition is a Dirichlet boundary condition ($u = 0$). The velocity parallel to the boundaries follows a Neumann boundary condition ($\partial u/\partial n = 0$, where n is normal to the boundary). The Neumann condition allows liquid to slide along the boundary.
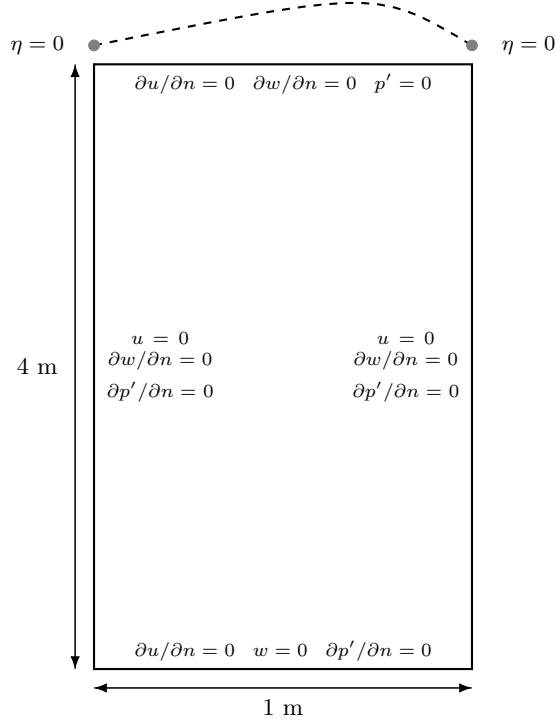

Figure 5: Schematic depicting the different boundary conditions imposed along the domain boundaries.

The boundary described above is a free-slip boundary. In a free-slip boundary, fluid can slide freely along the boundary as it is a Neumann BC. Alternatively, some runs use a no-slip boundary where a Dirichlet BC is imposed on both axes of the velocity vector.

One of the features of the solver is the inclusion of a free surface. Simply put, the free surface

is designed to simulate the behavior of the ocean surface. As the free surface is able to move, its boundary conditions are both Neumann to allow flow across it.

Along with the improved BCs, the domain size was chosen to be 1m by 4m to better represent a laboratory-scale environment as well. The same setup was used with a more classical solver in [3].

3.3 CFL violations

Numerical solvers come with a restriction; if the temporal resolution is too low relative to the spatial resolution, the simulation will develop oscillations that grow unbounded in time. The intuition behind this restriction is that numerical information can never be propagated faster than the physics of the problem allows—the time step must be sufficiently small such that the fluid physics can be captured by the discretization. The violation of this condition is referred to as the Courant–Friedrichs–Lewy (CFL) violation.

In order to satisfy the CFL condition, Eq.9 must be true for a C_{max} value of 1.

$$C = \frac{u \cdot \Delta t}{\Delta x_{eff}} + \frac{w \cdot \Delta t}{\Delta y_{eff}} \leq C_{\max} \qquad (9)$$

where Δx_{eff} and Δy_{eff} are defined in terms of the number of elements along the x-axis N_x, the number of elements along the z-axis N_z and the solution order p as,

$$\Delta x_{eff} = \frac{\Delta x}{p} = \frac{L}{N_x p} \qquad\qquad \Delta y_{eff} = \frac{\Delta y}{p} = \frac{H}{N_y p} \qquad (10)$$

During testing, the simulation was run at a scale of 1m by 4m with a resolution of 20 by 80. The final runs were run at a resolution of 40 and 160. The polynomial order (p) for both runs was 3.
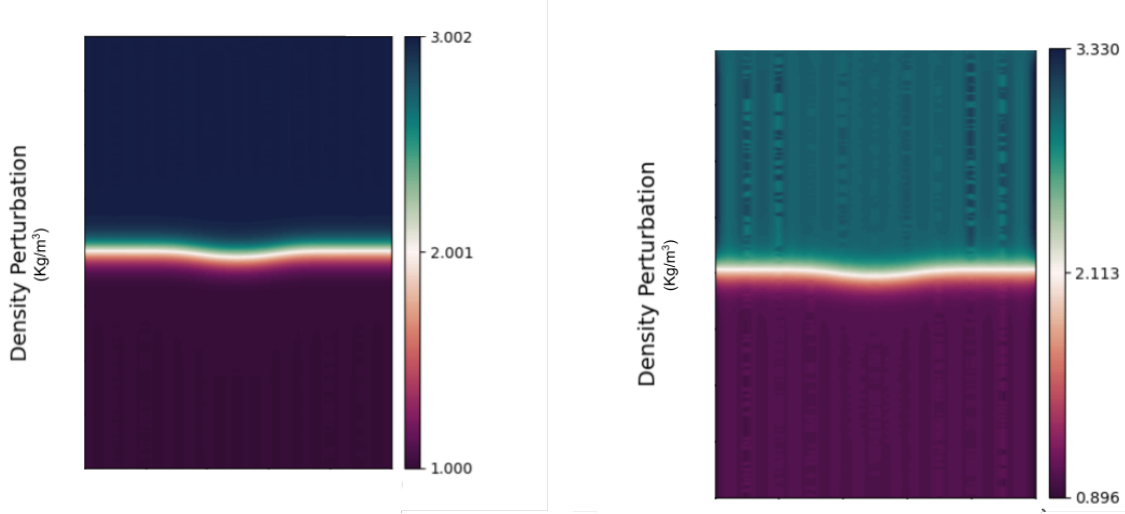
Figure 6: Before and After a CFL Violation. The left diagram was taken at $t = 0.012$ and has a C value of 0.0651 and the right was taken at $t = 0.012$ and has a C value of 6.3217

While low resolutions are a major factor for CFL violation, both the initial conditions along with different diffusivity values can reduce the value of C. The previous perturbation function, 8, was updated to provide smoother boundaries between the two densities.

$$\rho'(x, z) = \rho'_0 + \Delta\rho' \left[-\frac{1}{2} \tanh \left(N_z \left(-z + N_x \exp \left(-\frac{1}{2} \left(\frac{x - \frac{L}{2}}{\sigma} \right)^2 \right) \right) \right) + \frac{1}{2} \right] \quad (11)$$

The new equation for the density perturbation ρ' (11) along with an increased diffusivity value resulted in an increase in stability and mitigated the presence of CFLrelated instabilities.

3.4 Separate Diffusion

The importance of diffusivity was addressed in 3.3. However, the increase in diffusivity has certain adverse effects. At large diffusion values, changes in the density become dominated by the force of diffusion instead of the velocity created by the elevated denser fluid. We handle diffusion in our simulation in two parts. First, there is a tracer diffusion which represents the mixing force between fluids. Second, we also have diffusion applied to the momentum values, which is similar to the viscosity of the fluid, where a higher momentum diffusivity represents a higher viscosity. A higher diffusion value in the momentum equations reduces any oscillation while a higher tracer diffusion

reduces the density difference over time which reduces the buoyant force driving the RTI. In order to retain the stability granted by the momentum diffusion while reducing the tracer diffusivity, the values were separated and changed independently. This allowed for a stable simulation primarily governed by the force present in a Rayleigh-Taylor instability.

3.5   Relevant non-dimensional parameters

Our experiments have shown the importance of the following non-dimensional parameters on the underlying dynamics such as Atwood number and Ebsim number. Atwood number (Eq.12) is a dimensionless ratio between the densities of two liquids. Atwood Number can be used to characterize the behavior of RTIs as the difference in densities determine whether the vertical forcing term from 6 is significant. Ebsim number (Eq.13) is a dimensionless number that describes the relation between the buoyancy force and the viscosity of a liquid. Ebsim number helps predict how the down fluid will interact in the RTI. A large Ebsim value, such that $Eb \gg 1$, the physics becomes dominated by the buoyancy force and we expect that the RTI will resolve quickly with little mixing. Alternatively, when $Eb \ll 1$, the viscosity becomes the dominating force and by compression, the buoyancy becomes not dynamically important and by extension so does the vertical forcing term. However, when $Eb \approx 1$, there is a balance between both the viscosity and the buoyancy such that both are dynamically important and result in a more complex interaction between the two fluids as they move by each other.

$$A = \frac{\rho_2 - \rho_1}{\rho_2 + \rho_1} \tag{12}$$

$$Eb = \frac{\rho' g H^2}{\rho_0 \nu w} \tag{13}$$

which Eb is derived from the vertical forcing term and the diffusion in the momentum equations:

$$Eb = \frac{\frac{\rho'}{\rho_0} g}{\nabla \cdot (\nu \nabla w)} = \frac{\frac{\rho'}{\rho_0} g}{\frac{1}{H} \nu \frac{1}{H} w} = \frac{\rho' g H^2}{\rho_0 \nu w} \tag{14}$$

3.6   Preliminary results

Taking all of the considerations addressed above into account, we were able to effectively simulate and resolve the formation of RTIs at the laboratory scale. Figures 7 and 8 have $t = 0s, 40s, 80s, 120s, 160s$ and $200s$.
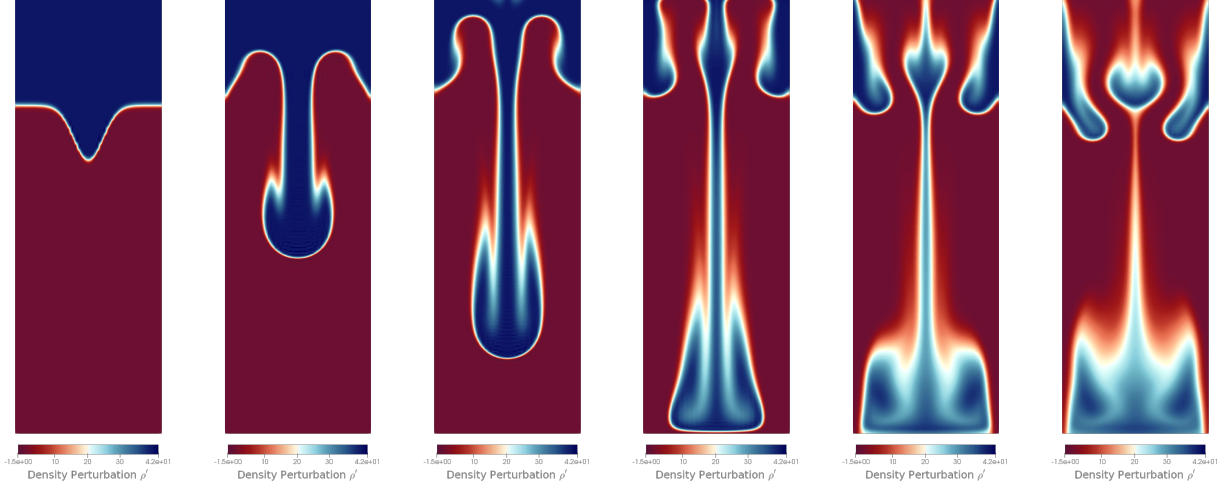

Figure 7: Rayleigh-Taylor instability with $N_x = 20, N_y = 80, \Delta t = 0.02$ and $\nu = 0.15$
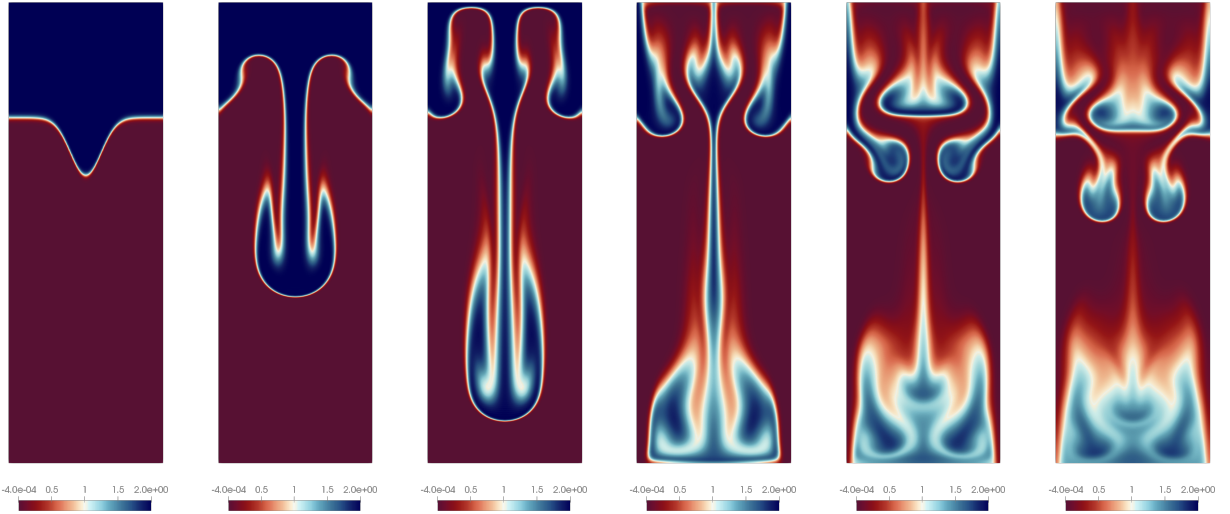

Figure 8: Rayleigh-Taylor instability with $N_x = 40, N_y = 160, \Delta t = 0.01$ and $\nu = 0.05$

11

4   Conclusion

In this paper, we succeeded in determining the requirements needed in order to simulate RTIs using an HDG-FEM. In particular, the importance of a vertical forcing term along with the effect of both the tracer diffusion and momentum diffusion. We noted how the Atwood number can be used as a predictor of whether the vertical forcing term is dynamically significant and how the Ebsim number of a simulation can be used to characterize the shape of the RTIs.

5   Future Work

While this paper began to examine the effect of different non-dimensional numbers affect the characteristics of the simulation, further work could be done to get a more comprehensive understanding.

6   Acknowledgments

I would like to thank my sponsor for allowing me to be able to attend RSI and meet all these amazing people.

Finally, thanks to my family for allowing me to attend the RSI conference as well as providing emotional support whenever I need it. You really are the world to me.

References

[1] T. Lolla, P. Haley Jr, and P. Lermusiaux. Path planning in multi-scale ocean flows: Coordination and dynamic obstacles. *Ocean Modelling*, 94:46–66, 2015.

[2] G. L. Russell, J. R. Miller, and D. Rind. A coupled atmosphere-ocean model for transient climate change studies. *Atmosphere-ocean*, 33(4):683–730, 1995.

[3] S. A. Khan and A. Shah. Simulation of the two-dimensional rayleigh-taylor instability problem by using diffuse-interface model. *AIP Advances*, 9(8), 2019.

[4] B. A. Remington, R. P. Drake, H. Takabe, and D. Arnett. A review of astrophysics experiments on intense lasers. *Physics of Plasmas*, 7:1641–1652, 2000.

[5] G. Boffetta and A. Mazzino. Incompressible Rayleigh-Taylor Turbulence. *Annual Review of Fluid Mechanics*, 49(1):119–143, 2017.

[6] D. L. Youngs. Numerical simulation of turbulent mixing by Rayleigh-Taylor instability. *Physica D: Nonlinear Phenomena*, 12(1):32–44, 1984.

[7] C. Keith. An investigation of nonhydrostatic flows with a high-order hybridizable discontinuous galerkin model. 2022.

[8] C. Foucart. *High-order Discontinuous Galerkin Methods and Deep Reinforcement Learning with Application to Multiscale Ocean Modeling*. PhD thesis, Massachusetts Institute of Technology, Department of Mechanical Engineering and Computational Science and Engineering, Cambridge, Massachusetts, Sept. 2023.

[9] C. Foucart, C. Mirabito, P. J. Haley, and P. F. Lermusiaux. High-order discontinuous galerkin methods for nonhydrostatic ocean processes with a free surface. In *OCEANS 2021: San Diego–Porto*, pages 1–9. IEEE, 2021.

[10] J.-L. Guermond, P. Minev, and J. Shen. An overview of projection methods for incompressible flows. *Computer methods in applied mechanics and engineering*, 195(44-47):6011–6045, 2006.

A Temporal discretization

Since our problem is in two spatial dimensions, we have the following dimension-specific temporal discretization of the underlying mathematical model. We consider the simulation time interval $[0, T]$ partitioned into equally-spaced time steps Δt, with each time step indexed by the integer k such that the current simulation time $t = (k + 1)\Delta t$. Therefore we write the temporal discretization such that we evolve all state variables from time step k to $k + 1$. The details of the spatial discretization are outside of the scope of this project and have been omitted for brevity. We refer the reader to [9] for details.

A.0.1 Velocity predictor:

The predictor velocity $\bar{\boldsymbol{u}}^{k+1} = [\bar{u}, \bar{w}]$ equations follow directly from the momentum equations, with the viscous diffusion terms treated implicitly; the nonlinear advective terms and forcing terms are treated explicitly.

$$
\frac{\partial \bar{u}^{k+1}}{\partial t} - \frac{\partial}{\partial x}\left(\nu_x \frac{\partial \bar{u}^{k+1}}{\partial x}\right) - \frac{\partial}{\partial z}\left(\nu_z \frac{\partial \bar{u}^{k+1}}{\partial z}\right)
$$
$$
= -\frac{\partial p'^{,k}}{\partial x} - g\frac{\partial \eta^k}{\partial x} - \frac{g}{\rho_0}\int_z^{\eta^k} \frac{\partial \rho'^{,k}}{\partial x}\, dz' - \nabla \cdot \left(u^k \otimes \boldsymbol{u}^k\right) - \frac{1}{\rho_0}f_x \tag{15}
$$
$$
\frac{\partial \bar{w}^{k+1}}{\partial t} - \frac{\partial}{\partial x}\left(\nu_x \frac{\partial \bar{w}^{k+1}}{\partial x}\right) - \frac{\partial}{\partial z}\left(\nu_z \frac{\partial \bar{w}^{k+1}}{\partial z}\right) = -\frac{\partial p'^{,k}}{\partial z} - \nabla \cdot \left(v^k \otimes \boldsymbol{u}^k\right) - \frac{\rho'^{,k}}{\rho_0}g - \frac{1}{\rho_0}f_z
$$

We remark that the additional vertical forcing term $\rho'^{,k}g/\rho_0$ has been retained in the vertical momentum equation by removing the contribution due to the density perturbation in 5.

A.0.2 Free-surface correction and intermediate projection:

We first solve for a correction to the free-surface in order to respect the depth-averaged continuity equation and perform a projection removing the component of the stage-final divergence corresponding to the free surface pressure.

$$
\frac{\delta \eta^{k+1}}{a\Delta t} - \nabla \cdot \left(a\Delta t g \left(\eta^k + H\right)\nabla \delta \eta^{k+1}\right) = -\nabla \cdot \int_{-H}^{\eta^k} \bar{u}^{k+1}\, dz \tag{16}
$$

$$
\bar{\bar{u}}^{k+1} = \bar{u}^{k+1} - a\Delta t g\frac{\partial}{\partial x}\delta \eta^{k+1} = \bar{u}^{k+1} - \frac{q_{\delta\eta,\,x}^{k+1}}{H + \eta^k}
$$
$$
\bar{\bar{w}}^{k+1} = \bar{w}^{k+1} \tag{17}
$$
$$
\eta^{k+1} = \eta^k + \delta \eta^k
$$

A.0.3 Pressure correction and projection:

Second, we perform a classical pressure projection step [10] in order to project the stage-final velocities into the space of divergence-free vector fields.

$$
-\nabla \cdot \left(\nabla \delta p'^{,k+1}\right) = -\frac{\nabla \cdot \bar{\bar{\boldsymbol{u}}}^{k+1}}{a\Delta t} \tag{18}
$$

$$\boldsymbol{u}^{k+1} = \bar{\bar{\boldsymbol{u}}}^{k+1} - a\Delta t \nabla \delta p'^{,k+1}$$

$$p'^{,k+1} = p'^{,k} + \delta p'^{,k+1}$$

$$(19)$$

At this point, the stage-final velocities $\boldsymbol{u}^{k+1}$ and nonhydrostatic pressure $p'^{,k+1}$ have been obtained.

A.0.4 Density perturbation update:

Having solved for the velocity state variables, we use them to update the density perturbation by solving auxiliary convection–diffusion problem. This completes the temporal discretization.

$$\frac{\partial \rho'^{,k+1}}{\partial t} - \nabla \cdot \left(\kappa \nabla \rho'^{,k+1} \right) = -\nabla \cdot \left(\boldsymbol{u} \rho'^{,k} \right) + f_{\rho'}. \tag{20}$$